Interplay of octahedral rotations and breathing distortions in charge-ordering perovskite oxides

Prasanna V. Balachandran and James M. Rondinelli*
Department of Materials Science and Engineering, Drexel University, Philadelphia, Pennsylvania 19104, USA
(Received 4 March 2013; published 1 August 2013)

We investigate the structure-property relationships in ABO_3 perovskites exhibiting octahedral rotations and cooperative octahedral breathing distortions (CBD) using group theoretical methods. Rotations of octahedra are ubiquitous in the perovskite family, while the appearance of breathing distortions—oxygen displacement patterns that lead to approximately uniform dilation and contraction of the BO_6 octahedra—are rarer in compositions with a single, chemically unique B site. The presence of a CBD relies on electronic instabilities of the B-site cations, either orbital degeneracies or valence-state fluctuations, and often appear concomitant with charge order metal-insulator transitions or B-site cation ordering. We enumerate the structural variants obtained from rotational and breathing lattice modes and formulate a general Landau functional describing their interaction. We use this information and combine it with statistical correlation techniques to evaluate the role of atomic scale distortions on the critical temperatures in representative charge ordering nickelate and bismuthate perovskites. Our results provide microscopic insights into the underlying structure-property interactions across electronic and magnetic phase boundaries, suggesting plausible routes to tailor the behavior of functional oxides by design.

DOI: 10.1103/PhysRevB.88.054101 PACS number(s): 61.50.Ks, 31.15.xh, 71.30.+h

I. INTRODUCTION

Perovskite oxides with chemical formula ABO_3 and B-site transition metal (TM) cations exhibit a range of functional electronic transitions that are intimately tied to the structure of the fundamental building blocks:[1] (i) the number of unique B–O bonds within an octahedron and (ii) the tilting of corner-connected octahedra. Adjacent BO_6 units typically fill space in perovskites through nearly rigid rotations, which produce deviations of the B–O–B bond angles away from the ideal 180° found in the cubic aristotype ($Pm\bar{3}m$ symmetry); the rotations are described by two three-dimensional irreducible representations (irreps), M_3^+ and R_4^+, of the high-symmetry structure.[2] Combinations of these lattice instabilities—cooperative bond length distortions and octahedral rotations—interact across *structural* phase transitions through elastic stresses and symmetry allowed coupling invariants as described within Landau theory.

Beside changes to crystal symmetry, the transition from high temperature (high symmetry) to low temperature (low symmetry) can also produce *electronic* metal-insulator (MI) transitions. Perovskite oxides with B-site cations in $t_{2g}^3e_g^1$ (d^4), $t_{2g}^6e_g^1$ (d^7), and $t_{2g}^6e_g^3$ (d^9) electronic configurations are particularly susceptible, because the low-energy electronic structure is dictated by the octahedral crystal-field split antibonding e_g orbitals—the atomiclike d-states that are spatially directed at the coordinating oxygen ligands. MI transitions, which occur simultaneously with lattice distortions, are common in low-dimensional materials, e.g., Peierls systems.[3] In three-dimensional perovskite oxides, however, the most familiar electronic transitions with concomitant changes in the B–O bond lengths and octahedral rotations result from cooperative first-order Jahn-Teller effects; tetragonal elongations of the BO_6 octahedra occur to remedy the orbital degeneracies that *localized* electrons encounter for particular B-site cation configurations, and through these distortions, the crystal maintains a uniform TM valence among all B sites across the transition.[4] The Jahn-Teller distortions are described by irreps Γ_3^+, M_2^+, and R_3^+, and their interaction with octahedral rotations are well-established.[5,6]

Unusually high-valence states or e_g^1 electrons in *delocalized* band states will also produce structural distortions, but in most cases will preserve the uniformity of the B–O bonds and the octahedral crystal field of the BO_6 units in the process.[7] The B cations will readily adopt mixed valence configurations, e.g., doped perovskites manganites[8] (containing nominally both Mn^{3+} and Mn^{4+}) and also stoichiometric nickelates[9] (Ni^{3+}) and ferrates[10] (Fe^{4+}). The TM cation will not maintain an integer valence state (n) uniformly on all B sites, but rather charge disproportionate (CDP), the simplest case being into two sites as

$$2B^{n+} \rightleftharpoons B^{(n-\delta)+}_{\text{site1}} + B^{(n+\delta)+}_{\text{site2}},$$

where δ is a fraction of an electron transferred between B sites. Electronic correlation and on-site Coulomb repulsion effects will prefer to order the valence deviations δ so that the inequivalent lattice sites, 1 and 2, form a periodic arrangement, changing the translational symmetry. This so-called *charge ordering* (CO) lowers the potential energy of the crystal and gaps the Fermi surface.[11] The electronic charge ordering is distinguishable[12–14] by an associated structural change in the local BO_6 building blocks (see Fig. 1). It appears as a B–O bond disproportionation or "breathing distortion," which causes the octahedra to either dilate (site 1) or contract (site 2) according to the charge δ transferred between sites,[15] largely because of the change in ionic radii, i.e., the effective radius of $B^{(n-\delta)+}$ is larger than $B^{(n+\delta)+}$.

The magnitude of the octahedral rotations is modified by these changes in the B-O bond lengths. The extent to which cooperation between octahedral breathing and rotation instabilities is necessary to stabilizing charge order and MI-transitions, however, is not as well understood[10,16] as the role of Jahn-Teller distortions on electronic transitions.[5,6,17] To this end, group

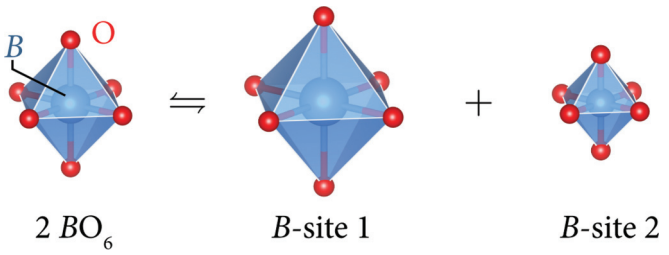

FIG. 1. (Color online) Illustration of the effect of charge disproportionation (CDP) on the local BO_6 octahedral site equivalence. Before the CDP transition, all octahedra are equivalent (left); afterwards, the BO_6 octahedra disproportionate into nonequivalent sites with the simplest two-site case shown here: charge transfer between B sites causes one octahedron to dilate (site 1) and the other octahedron to contract (site 2), resembling a "breathing" mode of the BO_6 perovskite building blocks.

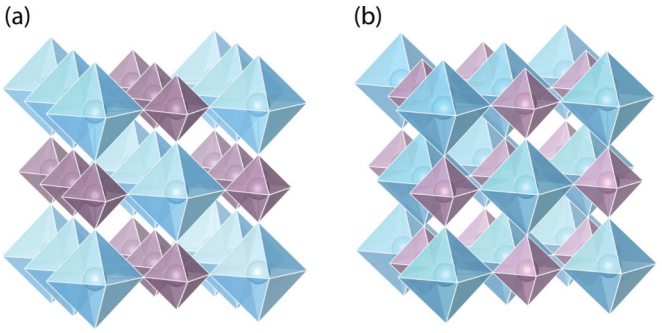

FIG. 2. (Color online) Schematic octahedral representations of the two cooperative structural breathing distortions that coexists with charge ordering in ABO_3 perovskites. In (a), the breathing distortion is two-dimensional, irrep M_1^+, and produces a columnar ordering of the two B cations reducing the symmetry to $P4/mmm$. In (b), a three-dimensional ordering produces a checkerboard arrangement of the B cations and is described by the R_1^+ irrep ($Fm\bar{3}m$ symmetry).

theoretical methods are particularly powerful to address the interactions among the multiple octahedron-derived instabilities. They provide a rigorous means to evaluate the symmetry allowed interactions between coupled lattice degrees of freedom, and thus, glean insight into the microscopic atomic structural contributions in the electronic CO transition in perovskite oxides.

In this work, we enumerate the space group and order parameter relationships for the octahedral breathing distortions, which are associated with irreps M_1^+ and R_1^+ of the aristotype cubic phase and the 15 simple octahedral rotation patterns available to bulk ABO_3 perovskites. We provide a list of symmetries that perovskite oxides with charge order tendencies and octahedral rotations could adopt—not all linear combinations of the instabilities are anticipated to be symmetry allowed.[18] Using this information, we then illustrate how to quantify relative contributions of octahedral breathing distortions and rotations across phase boundaries in prototypical nickelate and bismuthate perovskites. This rigorous mapping of the unit-cell level structural distortions into a symmetry-adapted basis enables us to disentangle the role that the *atomic structure* plays in directing the macroscopic *electronic* metal–insulator transitions. Finally, we show that a synergistic combination of group-theoretical analysis with statistical analysis makes it possible to understand the complex interplay pervasive in mixed-metal perovskite oxides.

II. COOPERATIVE BREATHING DISTORTIONS

The octahedral breathing distortions, which create two unique crystallographic B sites, must tile in three dimensions to maintain the corner connectivity of the BO_6 framework—the defining feature of the perovskite crystal structure. Here, we consider B–O distortions with wave vectors commensurate with the $Pm\bar{3}m$ lattice periodicity, i.e., those modes which occur on the edges and corners of the simple cubic Brillouin zone. The two main *cooperative* breathing distortions (CBD) are illustrated in Fig. 2. Note that the irreps, which we describe next, are defined using the $Pm\bar{3}m$ setting of the ABO_3 perovskite with the B cation located at the origin.[19]

The first type of CBD consists of two BO_6 building blocks, which are tiled to form a columnar arrangement of dilated and contracted octahedra [see Fig. 2(a)] that splits the B–O bond lengths into a doublet and quartet.[20] This distortion is associated with the active three-dimensional irrep M_1^+ with order parameter $(a,0,0)$ and manifests as a zone edge $k = (\frac{1}{2},\frac{1}{2},0)$ lattice instability of the cubic phase. The order parameter (OP) describes a vector in the irrep space and corresponds to specific directions along which the physical distortion may be induced. For the M_1^+ irrep, the OP can have three general components (a,b,c), where the values a, b, and c correspond to amplitudes of the two-dimensional breathing distortion along each Cartesian direction x, y, and z, respectively. Here, we consider only the case where $b = c = 0$, i.e., a restricted one-dimensional space. The possible directions for the OP correspond to $(a,0,0)$, $(0,a,0)$, and $(0,0,a)$ or columnar arrangements of the CBD along the x, y, and z directions, respectively, so that the octahedra distort in the same sense along the given direction. As a result, the symmetry is reduced to tetragonal, $P4/mmm$ (space group No. 123), and the B-site Wyckoff position of the cubic aristotype is split as $1a \rightarrow 1a + 1c$, doubling the number of perovskite formula units (f.u.) in the primitive cell (see Table I).

The second CBD consists of BO_6 octahedra that are tiled in a three-dimensional checkerboard arrangement [see Fig. 2(b)]. The distortion is described by a one-dimensional irrep R_4^+ and occurs as a $k = (\frac{1}{2},\frac{1}{2},\frac{1}{2})$ zone-corner lattice instability. Consequently, in the absence of other distortions, the CBD lifts the B-site equivalence while maintaining the O_h symmetry of the octahedra through uniform contraction and elongation of the B–O bonds about the trigonal axis, splitting the B-site Wyckoff position and forming a larger unit cell (see Table I). We note that this type of B-site ordering is common in double perovskites with multiple B cations that show large ionic size and/or considerable oxidation state differences, e.g., Ba_2MgWO_6.[21] However here, we consider only single (chemical species) B cations with different nominal valences.

TABLE I. Crystallographic data including the occupied Wyckoff positions (Wyck. site) for the cooperative breathing distortions (CBD) available to ABO_3 perovskites (see Fig. 2) in the absence of BO_6 rotations. Atom positions are given relative to the ideal cubic symmetry such that the relevant CBD imposed on the oxygen positions is indicated by Δ. The value of Δ controls the amplitude of the B–O contraction (elongation) and typically scales with the amount of intersite charge transfer (δ). The change in cell size is given relative to the pseudocubic (pc) lattice constant a_{pc}.

M_1^+ $(a,0,0)$ $P4/mmm$ (No. 123)		$a=b\sim\sqrt{2}a_{pc}, c\sim a_{pc}$ $\alpha=\beta=\gamma=90^\circ$		
Atom	Wyck. site	x	y	z
A	$2e$	0	$\frac{1}{2}$	$\frac{1}{2}$
$B(1)$	$1a$	0	0	0
$B(2)$	$1c$	$\frac{1}{2}$	$\frac{1}{2}$	0
O(1)	$4j$	$\frac{1}{4}+\Delta$	$\frac{1}{4}+\Delta$	0
O(2)	$1b$	0	0	$\frac{1}{2}$
O(3)	$1d$	$\frac{1}{2}$	$\frac{1}{2}$	$\frac{1}{2}$
$R_1^+(a)$ $Fm\bar{3}m$ (no. 225)		$a=b=c\sim 2a_{pc}$ $\alpha=\beta=\gamma=90^\circ$		
Atom	Wyck. site	x	y	z
A	$8c$	$\frac{1}{4}$	$\frac{1}{4}$	$\frac{1}{4}$
$B(1)$	$4a$	0	0	0
$B(1)$	$4b$	$\frac{1}{2}$	$\frac{1}{2}$	$\frac{1}{2}$
O	$24e$	$\frac{1}{4}+\Delta$	0	0

III. OCTAHEDRAL ROTATION AND CBD SPACE GROUPS

A. Methodology

To enumerate the allowed combinations of CBD and octahedral rotations in perovskite oxides, we use the group theoretical program ISOTROPY.[22] We follow the approach of Stokes *et al.*[23] and consider the changes in lattice symmetry due to the superposition of each CBD pattern (see Fig. 2) with the 15 octahedral rotation systems derived from the M_3^+ and R_4^+ three-dimensional irreps describing rotations.[2] The advantage of this approach is that group-subgroup relationships can be established between structural variants, enabling the understanding of the structural and electronic CO transitions within a first- or second-order theory. It should be noted that the analysis of *charge* order at a particular site in the crystal is effectively the same as analyzing the effects of *cation* order due to an order-disorder transition, because both valence and chemical species split a Wyckoff position identically. In the latter case, the irrep describes a "composition" mode and reflects the site occupancy.

In this work, we enumerate those mode combinations with well-defined cooperative breathing distortions that are most likely to be observed experimentally. Although the rock salt B cation order has been studied previously in ABO_3 perovskites, the layered ordering of B cations, i.e., irrep M_1^+, was examined only for the compositionally complex quadruple perovskite $A_4BB'_3O_{12}$ oxides.[24] Here, we report the results of the M_1^+ irrep on simple ABO_3 perovskites in the context of the CBD behavior, where cell-doubling occurs. Specifically for the M_1^+ irrep, we retain only those structures with an OP $(a,0,0)$ such that the second and third vector components are zero, unless an octahedral rotation permits it to be nonzero by symmetry. Furthermore, we follow the convention introduced in Refs. 2 and 25 and only keep structures with coherent rotations—those with a fixed "sense" about each axis. We remove structure variants from our analysis that would allow for a modulation in the amplitude and sense of the rotations about a single axis.

B. Space groups

We enumerate the space groups (see Table II) and associated octahedral tilt pattern, irreps, lattice vectors, and origin allowed by group theory. We follow Glazer's established notation[26] to denote the magnitude and phase of octahedral tilt patterns in perovskites. The description of octahedral rotations is encoded using the syntax $a^\#b^\#c^\#$, where letters a, b, and c indicate rotations of BO_6 units of equal or unequal magnitude about Cartesian x, y, and z axes. Note that in the case of equal magnitude rotations about different axes, the equivalent letter is duplicated, e.g., $a^\#a^\#a^\#$. The superscript # can take three values: 0, +, or −, for no rotations, in-phase rotations (neighboring octahedra along a Cartesian axis rotate in the same direction), or out-of-phase rotations (adjacent octahedra rotate in the opposite direction), respectively.

Table II provides the possible space-group symmetries compatible with CBD and octahedral rotations. The structural data are divided into three main blocks: the first section contains the space-group symmetries in the absence of CBD, the second section enumerates the symmetries that result from the planar CBD with octahedral rotations, and the third section includes those obtained from the three-dimensional CBD combined with rotations. Structures appearing in bold in Table II correspond to CBD without any octahedral rotations and are given first at the top of block two and three. Note that for perovskites with rotations and the M_1^+ CBD, there may be more than one structure possible for a given rotation, because the relative orientation of the tilt pattern with respect to the columnar arrangement of dilated and contracted octahedra alters the crystal symmetry differently.

Table II directly reveals the effect of the superposition of octahedral rotation patterns and the CBD patterns on the crystal symmetry lowering. Consider the middle block $(M_1^+\oplus M_3^+\oplus R_4^+)$. The seemingly similar tilt patterns $a^0a^0c^+$ and $a^+a^0c^0$, depending on the crystallographic axes they act upon, yield two different space groups, $P2/m$ and $Imma$, respectively.

Furthermore, there are a number of space groups appearing in each of the blocks of Table II: $C2/m$ appears both in the rotation only block (*sans* any CBD) and in the third block with the R_1^+ CBD. Formally, the crystallographic symmetries are identical in each case; however, physically, the rotation patterns adopted by the crystals are different. For instance, when only rotations associated with irrep R_4^+ and order parameter $(a,0,b)$ are present in the crystal structure, space group $C2/m$ allows the out-of-phase rotations about the y and z axes to be of different magnitude (tilting pattern is $a^0b^-c^-$). Now, consider the direct sum $R_1^+\oplus R_4^+$ for a vector space corresponding to the order parameter $(a,b,b,0)$ that

includes CBD. Even though the resulting space group is $C2/m$, the corresponding octahedral tilt pattern changes to $a^0b^-b^-$, where the out-of-phase rotations about the y and z axes are of the same magnitude. On the other hand, the direct sum $M_1^+ \oplus R_4^+$ for a vector space corresponding to the order parameter $(a,0,0,b,c,0)$ is found to preserve the $a^0b^-c^-$ tilting pattern, but the overall symmetry reduces to $C2/c$. Also note that, in the case of rotations without CBD, the tilt pattern $a^0b^-b^-$ corresponds to the higher symmetry $Imma$ space group. Such restrictions imposed on the rotation axes equivalence are described next, and for the reason previously described explains why "none" appears as an entry in Table III.

C. Compatible CBD and rotation symmetries

In Table III, we aggregate the results of the change in space-group symmetry due to the superposition of tilt patterns of M_1^+ and R_1^+ irreps with each of the 15 simple octahedral

TABLE II. Possible crystallographic space groups, octahedral rotation patterns, and unit-cell relationships for ABO_3 perovskites exhibiting rotations of octahedra given by irreps M_3^+ and R_4^+ with order parameter directions given in parentheses (η_i,η_j,η_k) with the CBD M_1^+ or R_1^+. The lattice vectors and origin shifts are given with respect to the high symmetry five-atom $Pm\bar{3}m$ structure (B cation at the origin).

		Order parameter direction				
space group	tilt pattern		M_3^+	R_4^+	lattice vectors	origin
221 $Pm\bar{3}m$	$a^0a^0a^0$		(0,0,0)	(0,0,0)	(1,0,0),(0,1,0),(0,0,1)	(0,0,0)
127 $P4/mbm$	$a^0a^0c^+$		(a,0,0)	(0,0,0)	(1,1,0),($\bar{1}$,1,0),(0,0,1)	(0,0,0)
139 $I4/mmm$	$a^0b^+b^+$		(a,0,a)	(0,0,0)	(0,2,0),(0,0,2),(2,0,0)	($\frac{1}{2},\frac{1}{2},\frac{3}{2}$)
204 $Im\bar{3}$	$a^+a^+a^+$		(a,a,a)	(0,0,0)	(2,0,0),(0,2,0),(0,0,2)	($\frac{1}{2},\frac{1}{2},\frac{1}{2}$)
71 $Immm$	$a^+b^+c^+$		(a,b,c)	(0,0,0)	(2,0,0),(0,2,0),(0,0,2)	($\frac{1}{2},\frac{1}{2},\frac{1}{2}$)
140 $I4/mcm$	$a^0a^0c^-$		(0,0,0)	(a,0,0)	(1,1,0),($\bar{1}$,1,0),(0,0,2)	(0,0,0)
74 $Imma$	$a^0b^-b^-$		(0,0,0)	(a,0,a)	(0,1,1),(2,0,0),(0,1,$\bar{1}$)	(0,0,0)
167 $R\bar{3}c$	$a^-a^-a^-$		(0,0,0)	(a,a,a)	($\bar{1}$,1,0),(0,$\bar{1}$,1),(2,2,2)	(0,0,0)
12 $C2/m$	$a^0b^-c^-$		(0,0,0)	(a,0,b)	(0,$\bar{2}$,0),(2,0,0),(0,1,1)	($\frac{1}{2},\frac{1}{2}$,0)
15 $C2/c$	$a^-b^-b^-$		(0,0,0)	(a,b,a)	(2,$\bar{1}$,$\bar{1}$),(0,1,$\bar{1}$),(0,1,1)	($\frac{1}{2},\frac{1}{2}$,0)
2 $P\bar{1}$	$a^-b^-c^-$		(0,0,0)	(a,b,c)	(0,1,1),(1,0,1),(1,1,0)	(0,0,0)
63 $Cmcm$	$a^0b^+c^-$		(0,0,a)	(b,0,0)	(2,0,0),(0,0,$\bar{2}$),(0,2,0)	($\frac{1}{2}$,0,$\frac{1}{2}$)
62 $Pnma$	$a^+b^-b^-$		(0,a,0)	(b,0,b)	(0,1,1),(2,0,0),(0,1,$\bar{1}$)	(0,0,0)
11 $P2_1/m$	$a^+b^-c^-$		(0,a,0)	(b,0,c)	(0,$\bar{1}$,1),(2,0,0),(0,1,1)	(0,0,0)
137 $P4_2/nmc$	$a^+a^+c^-$		(0,a,a)	(b,0,0)	(2,0,0),(0,2,0),(0,0,2)	(0,0,$\bar{1}$)
		M_1^+				
127 $P4/mbm$	$a^0a^0c^{0a}$	(a,0,0)[b]	(0,0,0)	(0,0,0)	(1,1,0),($\bar{1}$,1,0),(0,0,1)	(0,0,0)
83 $P4/m$	$a^0a^0c^+$	(a,0,0)	(b,0,0)	(0,0,0)	(1,1,0),($\bar{1}$,1,0),(0,0,1)	(0,0,0)
74 $Imma$	$a^+a^0c^0$	(a,0,0)	(0,0,b)	(0,0,0)	(0,2,0),(0,0,2),(2,0,0)	(0,0,0)
69 $Fmmm$	$a^+a^+c^0$	(a,0,0)	(0,b,b)	(0,0,0)	(0,$\bar{2}$,0),(2,0,2),($\bar{1}$,1,1)	($\frac{1}{2},-\frac{1}{2},-\frac{1}{2}$)
12 $C2/m$	$a^+b^+c^+$	(a,0,0)	(b,c,d)	(0,0,0)	($\bar{2}$,2,0),(0,0,$\bar{2}$),(0,2,0)	($\frac{1}{2},-\frac{1}{2},\frac{1}{2}$)
124 $P4/mcc$	$a^0a^0c^-$	(a,0,0)	(0,0,0)	(b,0,0)	(1,1,0),($\bar{1}$,1,0),(0,0,1)	(0,0,0)
63 $Cmcm$	$a^-a^0c^0$	(a,0,0)	(0,0,0)	(0,b,b)	(0,2,0),(0,0,2),(2,0,0)	(0,0,0)
51 $Pmma$	$a^-a^-c^0$	(a,0,0)	(0,0,0)	(0,b,b)	(0,0,2),(1,1,0),($\bar{1}$,1,0)	(0,0,0)
13 $P2/c$	$a^-a^-c^-$	(a,0,0)	(0,0,0)	(c,b,b)	(1,1,0),($\bar{1}$,1,0),(0,0,2)	(0,0,0)
15 $C2/c$	$a^0b^-c^-$	(a,0,0)	(0,0,0)	(b,c,0)	(2,0,0),(0,2,0),(0,0,2)	(0,0,0)
11 $P2_1/m$	$a^-b^-c^0$	(a,0,0)	(b',0,0)[c]	(0,c,d)	($\bar{1}$,1,0),(0,2,0),(1,1,0)	(0,0,0)
2 $P\bar{1}$	$a^-b^-c^-$	(a,0,0)	(b',0,0)[c]	(c,d,e)	(1,1,0),($\bar{1}$,1,0),(0,0,2)	(0,0,0)
52 $Pnna$	$a^0b^+c^-$	(a,0,0)	(0,0,b)	(c,0,0)	(0,0,2),(0,2,0),($\bar{2}$,0,0)	(0,0,0)
62 $Pnma$	$a^+b^-c^0$	(a,0,0)	(0,0,b)	(0,c,0)	(0,2,0),(0,0,2),(2,0,0)	(0,0,0)
11 $P2_1/m$	$a^-b^-c^+$	(a,0,0)	(b,0,0)	(0,c,d)	($\bar{1}$,1,0),(0,2,0),(1,1,0)	(0,0,0)
68 $Ccca$	$a^+a^+c^-$	(a,0,0)	(0,b,b)	(c,0,0)	(2,2,0),($\bar{2}$,2,0),(0,0,2)	(2,0,0)
		R_1^+				
225 $Fm\bar{3}m$	$a^0a^0a^{0d}$	(a)	(0,0,0)	(0,0,0)	(2,0,0),(0,2,0),(0,0,2)	(0,0,0)
128 $P4/mnc$	$a^0a^0c^+$	(a)	(b,0,0)	(0,0,0)	(1,1,0),($\bar{1}$,1,0),(0,0,2)	(0,0,0)
201 $Pn\bar{3}$	$a^+a^+a^+$	(a)	(b,b,b)	(0,0,0)	(0,0,$\bar{2}$),(0,$\bar{2}$,0),($\bar{2}$,0,0)	(1,1,1)
134 $P4_2/nnm$	$a^0b^+b^+$	(a)	(b,b,0)	(0,0,0)	(0,0,2),(2,0,0),(0,2,0)	(0,$\bar{1}$,0)
48 $Pnnn$	$a^+b^+c^+$	(a)	(b,c,d)	(0,0,0)	($\bar{2}$,0,0),(0,0,2),(0,2,0)	(0,0,0)
148 $R\bar{3}$	$a^-a^-a^-$	(a)	(0,0,0)	(b,b,b)	($\bar{1}$,1,0),(0,$\bar{1}$,1),(2,2,2)	(0,0,0)
87 $I4/m$	$a^0a^0c^-$	(a)	(0,0,0)	(b,0,0)	($\bar{1}$,1,0),($\bar{1}$,$\bar{1}$,1),(0,0,2)	(0,0,0)
12 $C2/m$	$a^0b^-b^-$	(a)	(0,0,0)	(b,b,0)	($\bar{1}$,2,1),(1,0,1),(0,2,0)	(0,0,0)

TABLE II. (*Continued.*)

space group	tilt pattern	Order parameter direction	M_3^+	R_4^+	lattice vectors	origin
2 $P\bar{1}$	$a^-b^-c^-$	(a)	(0,0,0)	(b,c,d)	(1,0,1),(1,1,0),($\bar{1}$,1,0)	(0,0,0)
15 $C2/c$	$a^0b^+c^-$	(a)	(b,0,0)	(0,0,c)	(2,0,0),(0,2,0),(0,0,2)	($\frac{1}{2}$,$\frac{1}{2}$,0)
86 $P4_2/n$	$a^+a^+c^-$	(a)	(b,b,0)	(0,0,c)	(0,0,2),(2,0,0),(0,2,0)	($\bar{1}$,$\bar{1}$,0)
14 $P2_1/c$	$a^+b^-b^-$	(a)	(b,0,0)	(0,c,c)	(1,$\bar{1}$,0),(1,1,0),(1,$\bar{1}$,2)	(0,0,0)

[a]In the absence of octahedral rotations, the axes are unique due to the CBD.
[b]The CBD makes the z-direction unique.
[c]The b' denotes that this is a secondary distortion that is symmetry allowed. In this case in-phase rotations about the z-direction. The Glazer tilt is defined for the case $b' = 0$.
[d]The R_1^+ mode acts along the body diagonal and does not create a unique axis in the crystal as in the case of the the three-dimensional M_1^+ irrep. Only the octahedral rotations lifts the axes equivalence.

tilt systems. This information is schematically shown in Fig. 3. Only one symmetry exists, $P\bar{1}$, where the breathing distortion is geometrically compatible with the symmetry of the perovskite structure with octahedral rotations alone ($a^-b^-c^-$), meaning "no change" in unit cell or translational symmetry is required to accommodate the multiple distortions. Table III also reveals that the $P2_1/m$ symmetry is compatible with two different octahedral rotation patterns and the M_1^+ CBD: $a^0b^-c^-$ and $a^+b^-c^-$. While $P\bar{1}$ is compatible with both M_1^+ and R_1^+ irreps, $P2_1/m$ only exists for the M_1^+ irrep.

For entries containing "none," the direct sums, $R_1^+ \oplus M_3^+ \oplus R_4^+$ and $M_1^+ \oplus M_3^+ \oplus R_4^+$, do not yield an isotropy subgroup. These results hold strictly for the superposition of tilt patterns associated with the order parameter directions explored in this work. Although, this does not preclude the likelihood for the material to adapt to a different tilt system, i.e., an order parameter direction not considered in our paper, which would then lower the crystal symmetry, thereby yielding an isotropy subgroup. This is made clear by examining the $a^-a^-a^-$ rotation pattern, which corresponds to an equal amplitude of out-of-phase rotations about each axis, or equivalently a single out-of-phase rotation about the threefold axis. The trigonal symmetry is incompatible with a distortion that would require a loss of the threefold axis and therefore need at a minimum a symmetry reduction to a lattice with tetragonal geometry. Thus "none" appears in the M_1^+ column corresponding to the row with the $a^-a^-a^-$ rotation pattern. Such incompatibility with the M_1^+ CBD is alleviated if the rotation pattern about any two crystallographic axes are of different magnitudes, e.g., $a^-b^-b^-$, yielding space group $P2/c$ (see Table III).

TABLE III. The change in space group which occurs when the different octahedral CBD patterns are superposed with the 15 simple octahedral tilt systems.

Tilt system (Glazer notation)	No Breathing	M_1^+	R_1^+
$a^0a^0a^0$	$Pm\bar{3}m$	$P4/mmm$	$Fm\bar{3}m$
$a^0a^0c^+$	$P4/mbm$	$P4/m$ $Imma$	$P4/mnc$
$a^0b^+b^+$	$I4/mmm$	$Fmmm$	$P4_2/nnm$
$a^+a^+a^+$	$Im\bar{3}$	none	$Pn\bar{3}$
$a^+b^+c^+$	$Immm$	$C2/m$	$Pnnn$
$a^0a^0c^-$	$I4/mcm$	$P4/mcc$ $Cmcm$	$I4/m$
$a^0b^-b^-$	$Imma$	$Pmma$	$C2/m$
$a^-a^-a^-$	$R\bar{3}c$	none	$R\bar{3}$
$a^0b^-c^-$	$C2/m$	$C2/c$	none
		$P2_1/m$	
$a^-b^-b^-$	$C2/c$	$P2/c$	none
$a^-b^-c^-$	$P\bar{1}$	no change	no change
$a^0b^+c^-$	$Cmcm$	$Pnna$ $Pnma$	$C2/c$
$a^+b^-b^-$	$Pnma$	none	$P2_1/c$
$a^+b^-c^-$	$P2_1/m$	$P2_1/m$	none
$a^+a^+c^-$	$P4_2/nmc$	$Ccca$	$P4_2/n$

IV. STRUCTURAL TRANSITIONS

Although the microscopic origin for charge disproportionation results from an electronic instability related to the electronic configuration of a particular metal center, the cooperative ordering of the CDP leads to a macroscopic bond

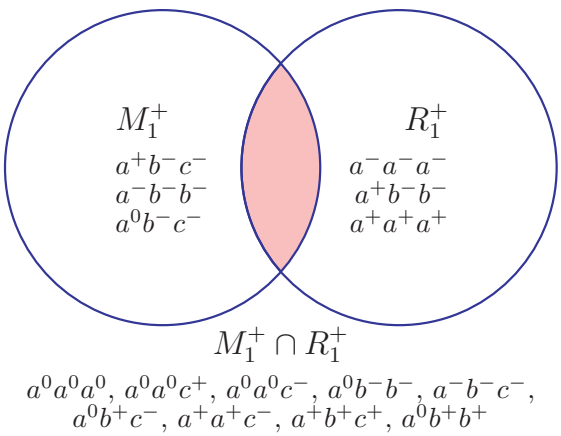

FIG. 3. (Color online) Representation of the rotation patterns that are compatible with each (or both, given by the intersection of the) CBD without requiring a further symmetry reduction.

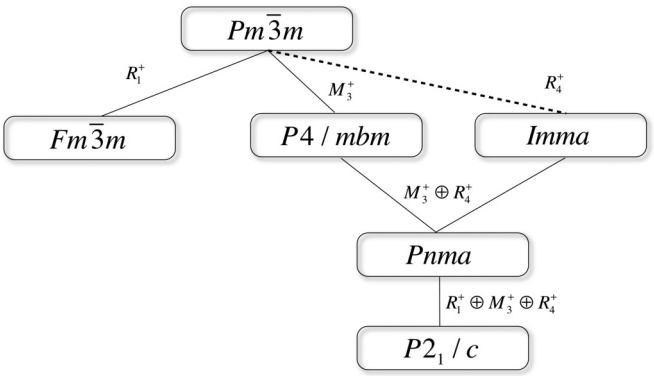

FIG. 4. Group-subgroup relationship between $Pm\bar{3}m$ and $P2_1/c$. Irreps within $Pm\bar{3}m$ responsible for transitions are shown. In addition, we note that $M_3^+ \oplus R_4^+ \oplus R_3^+$ and $M_3^+ \oplus R_4^+ \oplus M_5^+$ would also transform $Pm\bar{3}m \rightarrow P2_1/c$. Dotted line indicates that the phase transition is not allowed to be continuous within the confines of Landau theory.

disproportionation. In the displacive limit, the two unique and nearly uniform octahedra result, dilating and contracting in proportion to the magnitude of charge transfer. Across the electronic phase transitions, the breathing distortions can couple directly to octahedral rotations. (We do not consider here indirect coupling through a common strain component.)

Here we describe the effect of superposition of the common orthorhombic rotation pattern ($a^+b^-b^-$) obtained from irreps M_3^+ and R_4^+, which gives the six-dimensional order parameter with two unique directions as

$$(\eta_+,0,0,0,\eta_-,\eta_-)\,.$$

The superposition of the three-dimensional CBD R_1^+ and the rotation pattern gives a seven-dimensional order parameter space, i.e., $(\beta,\eta_+,0,0,0,\eta_-,\eta_-)$, which we contract to an effective four-dimensional space to obtain the $P2_1/c$ space group (cf. Table II). Without assuming which transition occurs first—whether the rotations precede or follow the CBD—we construct a Landau free energy expansion about the cubic phase ($\beta = \eta_+ = \eta_- = 0$) as

$$\mathcal{F}(\beta,\eta_i) = \phi^2 + \phi^4 + C_1\beta^2\eta_+^2 + C_2\beta^2\eta_-^2 + D_3\eta_+^2\eta_-^2\,,$$

where ϕ^2 and ϕ^4 describe the homogeneous quadratic and quartic terms for each order parameter, and C_i are the coefficients coupling the CBD to the in- or out-of-phase rotations, and D_3 describes the biquadratic coupling of the different BO_6 rotation "senses" in the $a^+b^-b^-$ tilt pattern. The group-subgroup relationships are depicted in Fig. 4.

The rotations and the CBD couple biquadratically, which indicates that the interactions across the transitions could be either cooperative or antagonistic. It is possible that the particular rotations could suppress CO by eliminating the structural octahedral breathing distortion altogether through the interaction terms containing the C_i coefficients. However, in most cases, the rotation amplitudes are weakly modified across the electronic CO transition, suggesting that the strength of the coupling C_i is in general small. We explore this in Sec. V through a statistical approach.

We also note that while the order of the coupling is important, the difference in temperature scales at which the rotation and charge ordering occurs is also important in determining how the structural order parameters influence each other. The strongest interaction occurs when the temperatures are similar, while if they are far apart, the two structural transitions will weakly couple.

V. STRUCTURE-FUNCTIONALITY RELATIONSHIPS

In this section, we apply our group theory results to quantitatively explore the relationship between structure and physical properties of experimentally known rare-earth nickelate and bismuthate perovskites. There is significant interest in developing strategies—both experimentally and theoretically—to rationally control octahedral distortions through the interplay of chemical pressure, epitaxial strain engineering, and ultrathin superlattice heterostructure formation[27–32] for property control. Although several octahedral distortion metrics, e.g., the crystallographic tolerance factor or bending of the B–O–B bond angle,[33,34] have played an important role in the understanding of the electronic and magnetic properties of perovskite oxides,[35] they have had limited success in materials design of nonthermodynamic phases in thin film geometries. Knowledge of quantitative structure–property octahedral distortion relationships are required to accelerate materials discoveries.

Distortion-mode decomposition analysis is an alternative approach[5,6,22,36] (widely practiced and followed in the crystallography literature) to study displacive[37] phase transitions in perovskites. It involves describing a distorted (low-symmetry) structure as arising from a (high-symmetry) parent structure with one or more static symmetry-breaking structural distortions.[36] In the undistorted parent structure, each symmetry breaking distortion-mode has zero amplitude. The low-symmetry phase, however, will have finite amplitudes for each irrep compatible with the symmetry breaking. Said another way, the low-symmetry phase is rigorously described through a series expansion of static symmetry breaking structural modes that "freeze" into the parent structure. Critically, the weights or amplitudes assigned to each irrep are obtained according to the contribution that each irrep is present *and* the requirement that linearity is maintained.

What is of particular utility in formulating quantitative relationships connecting octahedral distortions, which are now described mathematically, to macroscopic properties for materials design is that each irrep carries a physical representation of the displacive distortions—the unique atomic coordinates describing various symmetry-adapted structural modes. The relative importance of these modes on properties may then be mapped by means of *ab initio* computational methods.[38] Accessibility to computational methods make the distortion-mode analysis powerful, because it is possible to independently study various distortions and directly assess their role in structural and electronic phase transition mechanisms. Furthermore, the distortion-mode analysis relies solely on crystal structural data, which enables both bulk and thin film stabilized structures with identical compositions to be evaluated on equal footing. Such direct comparison is not possible through aggregate parameters such as the tolerance factor, i.e., when the composition is fixed, or other metrics widely followed in the literature.

In the remainder of this section, we use the distortion modes to form the basis for the quantitative description of octahedral distortions and CBD on material properties. Using bulk $R\mathrm{NiO_3}$, where R is a rare-earth element, and $\mathrm{Ba_{1-x}K_xBiO_3}$ perovskite compounds as prototypical charge-ordering materials, we decompose available low-symmetry structural data into symmetry-adapted structural distortion modes. We then evaluate and correlate the amplitudes of the distortion-modes to macroscopic materials behavior to uncover trends linking octahedral distortions to the structural and physical properties. We use the group-theory program ISODISTORT[22] for distortion-mode decomposition analysis and R[39,40] for the statistical analysis. For readers interested in reproducing our work, we have deposited the raw data and the R script in Supplemental Material.[41]

A. $R\mathrm{NiO_3}$ Nickelates

Rare-earth perovskite nickelates, $R\mathrm{NiO_3}$, where R = Y, Ho, Er, Dy, Lu, Pr, or Nd, exhibit nontrivial changes in structure and physical properties, including sharp first-order temperature-driven MI transitions, unusual antiferromagnetic order in the ground state, and site- or bond-centered charge disproportionation.[33,42,43] At the MIT temperature (T_{MI}), the crystal symmetry lowers from orthorhombic $Pnma$ to monoclinic $P2_1/c$ symmetry[44] (see Fig. 4), where the Ni cation no longer maintains a unique uniform valence on all sites, and disproportionates as

$$2\mathrm{Ni}^{3+} \rightleftharpoons \underset{\text{site1}}{\mathrm{Ni}^{(3-\delta)+}} + \underset{\text{site2}}{\mathrm{Ni}^{(3+\delta)+}}.$$

Moreover, the insulating ground-state displays a complex antiferromagnetic order (type E') below a Néel temperature (T_N). Several previous studies[33,34,45–48] have suggested the likely existence of a complex interplay between octahedral rotations, transport, and magnetic properties. To extract deeper insight into these interrelationships, we (i) identify all active distortion modes in each composition, (ii) determine the individual amplitudes for each modes, and (iii) explore the statistical correlation between individual distortion-modes and the physical properties, specifically T_{MI} and T_N.

1. Structure decomposition

We follow the procedure outlined by Campbell *et al.*[22] to decompose the $P2_1/c$ monoclinic crystal structure data, obtained from previously published diffraction studies,[49–52] into the orthonormal symmetry-modes. Diffraction data for $\mathrm{YNiO_3}$, $\mathrm{ErNiO_3}$, $\mathrm{LuNiO_3}$, and $\mathrm{HoNiO_3}$ were measured at 295 K, for $\mathrm{DyNiO_3}$ at 200 K, for $\mathrm{NdNiO_3}$ at 50 K, and finally for $\mathrm{PrNiO_3}$ at 10 K. T_{MI} and T_N were obtained from the review article by Catalan.[34]

The $P2_1/c$ structure decomposes into eight algebraically independent symmetry modes corresponding to the following irreps: R_1^+, R_3^+, R_4^+, R_5^+, X_5^+, M_2^+, M_3^+, and M_5^+. The relative amplitudes for each of the distortions are given in Table IV, with the physical representation of each irrep and its consequence on the octahedral framework schematically illustrated in Fig. 5.

The sequence of structures involved in the phase transition could be written as follows: $Pm\bar{3}m \rightarrow Pnma \rightarrow P2_1/c$.

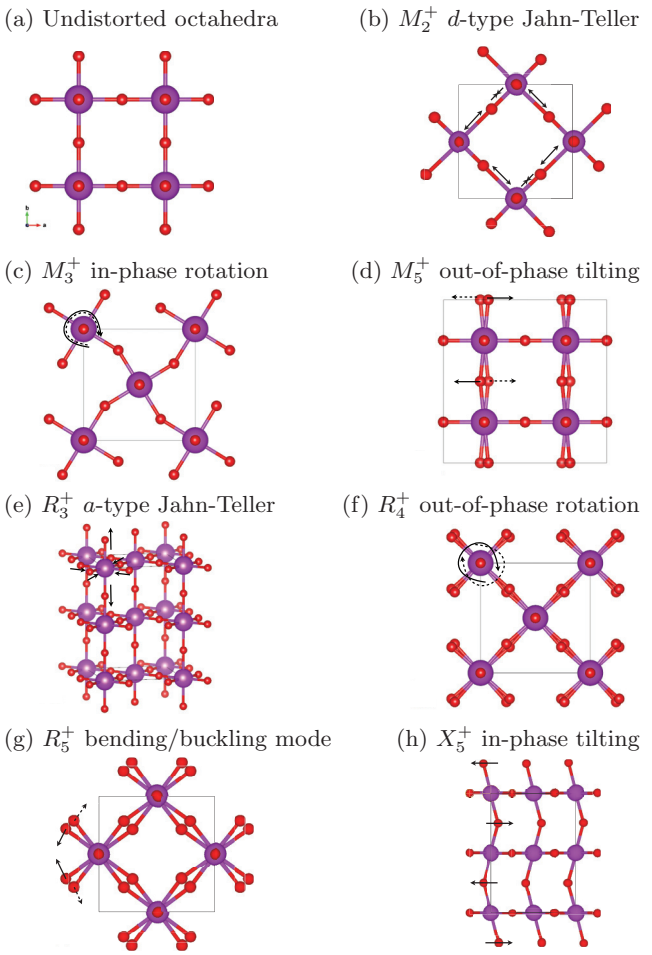

FIG. 5. (Color online) Illustration of the symmetry-adapted orthonormal distortion modes found in the low-symmetry $R\mathrm{NiO_3}$ and $\mathrm{Ba_{1-x}K_xBiO_3}$ perovskites. The undistorted octahedra are shown in (a) for comparison. Octahedral tilting distortions refer to the rotation of the octahedral units (we use "tilting" and "rotation" interchangeably). The out-of-phase distortions are differentiated using arrows (lines and dashes) indicating the direction of cooperative atomic displacements. (b) M_2^+ describes the d-type Jahn-Teller mode, where two bonds shrink and two elongate; (c) M_3^+ describes an in-phase rotation mode; (d) M_5^+ describes an out-of-phase tilting mode, which could also act as an in-phase tilting mode depending on the order parameter direction (e) R_3^+ describes the a-type Jahn-Teller mode, where four bonds contract and two expand, and vice versa; (f) R_4^+ describes an out-of-phase rotation mode; (g) R_5^+ describes an out-of-phase bending mode; and (h) X_5^+ describes an in-phase tilting mode accompanied by A cation displacements, which are not shown for clarity.

Five distortions participate in the $Pm\bar{3}m \rightarrow Pnma$ transition, namely R_4^+, R_5^+, X_5^+, M_2^+, and M_3^+. Within Landau theory, the $Pnma$ structure results from the condensation of two zone-boundary phonons of different wave vectors: one at the R point of the cubic Brillouin zone that transforms as the irrep R_4^+, and the other at the M point, which transforms as the irrep M_3^+. Not surprising, the two most common octahedral distortion modes that describe the $a^+b^-b^-$ rotation pattern, R_4^+ and M_3^+, emerge as the primary modes. A secondary mode with X_5^+ symmetry also appears with relatively high amplitude, and it contains A cation displacements. Such

TABLE IV. Summary of the amplitudes of each irrep (notation given with respect to the $Pm\bar{3}m$ parent space-group) in the $P2_1/c$ structure (units in Å). Std. err. $= \sigma/N$, where σ is the standard deviation and N (=7) is the sample size, gives an estimate of the sampling error. The total distortion amplitude is given in the column indicated by $\sum$.

	also present in $Pnma$								
RNiO$_3$	R_4^+	R_5^+	X_5^+	M_2^+	M_3^+	R_1^+	R_3^+	M_5^+	$\sum$
HoNiO$_3$	1.499	0.195	0.826	0.048	1.153	0.172	0.024	0.025	2.081
ErNiO$_3$	1.535	0.203	0.842	0.048	1.179	0.145	0.022	0.020	2.127
LuNiO$_3$	1.648	0.248	0.907	0.063	1.229	0.153	0.004	0.016	2.268
YNiO$_3$	1.502	0.196	0.835	0.055	1.161	0.128	0.011	0.072	2.089
NdNiO$_3$	1.179	0.117	0.445	0.030	0.751	0.126	0.050	0.283	1.505
PrNiO$_3$	1.093	0.063	0.362	0.004	0.690	0.091	0.012	0.000	1.347
DyNiO$_3$	1.442	0.207	0.780	0.073	1.144	0.241	0.025	0.168	2.041
Std. err.	0.029	0.009	0.031	0.003	0.032	0.007	0.002	0.015	–

antiparallel displacements of the A cations are established to be correlated with the amplitudes of the octahedral rotations in perovskites.[53]

In the symmetry lowering $Pnma \rightarrow P2_1/c$ structural phase transition, irrep R_1^+ with order parameter (a) is the primary order parameter capturing the CDP behavior. The R_3^+ and M_5^+ are secondary distortions in the phase transition that accompany R_1^+. This is seen in Table IV, where the largest amplitude for modes not already present from the transition to $Pnma$ is almost always given by R_1^+.

In the nickelate literature, generally NdNiO$_3$ is discussed in conjunction with PrNiO$_3$, because together they represent a unique case where $T_{\rm MI}$ and T_N coincide. In NdNiO$_3$, we find that the distortion amplitude for M_5^+ is twice that of R_1^+, indicating that irrep M_5^+ acts as the primary distortion mode instead of R_1^+. This involves splitting of the oxygen Wyckoff orbit (as present in the cubic perovskite structure) into two and the apical oxygen atoms (along the c axis) are displaced from their high-symmetry positions. Indeed, our group theoretical analysis shows that for the direct sum, $M_3^+ \oplus R_4^+ \oplus M_5^+$, whose tilt system corresponds to the order parameter containing only three free parameters: (a,0,0,0,b,b,c,c,0,0,c,$-c$), the required space group is $P2_1/c$ monoclinic structure, an isotropy subgroup of $Pnma$, indicating that M_5^+ could be the primary distortion mode in the phase transition if it also provides the greatest energetic stability to the structure. The latter constraint requires evaluation of the lattice dynamics using a technique beyond group theory. Interestingly, for the experimental bulk PrNiO$_3$ structure, irrep M_5^+ is found to have zero amplitude.

To summarize this discussion, we have introduced an alternative symmetry-mode description of the structural distortions in nickelates that identifies bulk NdNiO$_3$ compound as anomalous in the series. Combining temperature-dependent diffraction studies with mode decomposition analysis could provide key insights necessary to fully understand the evolution of the primary and secondary distortions with the thermodynamic origin of phase transition.

We now shift our attention to the weak secondary distortion modes, particularly to the observation of two types of Jahn-Teller distortions in the NiO$_6$ units, M_2^+ and R_3^+ (see Fig. 5). Although M_2^+ and R_3^+ are practically negligible and are the secondary distortion modes in the $Pm\bar{3}m \rightarrow Pnma \rightarrow P2_1/c$ transition, their presence could still have significant implications on the physical properties. The motivation for critically analyzing secondary distortion modes in nickelates comes from the study of *improper* phase transitions,[54–56] e.g., where spontaneous electric polarization arises as a secondary effect accompanying complex nonpolar distortions through anharmonic interactions[57–60] in improper ferroelectrics. Similarly, we are interested in exploring the role of secondary order parameters on the electronic properties of nickelates.

Experimental observations based on giant oxygen O^{16}-O^{18} isotope effect[45] indicate the presence of dynamic Jahn-Teller polarons; however, the interpretation of orbital-ordering has lacked conclusive support from diffraction experiments.[34] More recently, ultrathin films of nickelates are being increasingly investigated for rational control of orbital polarization.[61–63] The identification of Jahn-Teller bond elongations and contractions from our symmetry analysis in the bulk compounds suggests the nickelates should have tendencies to orbital (ordering) polarizations. Misfit strain, superlattice formation, or symmetry mismatch at the thin film-substrate interface may be used to selectively enhance the contributions of Jahn-Teller modes described by irreps M_2^+ and R_3^+, as recently proposed in Ref. 64. Alternatively, orbital-ordering could *emerge* in nickelates, e.g., LaNiO$_3$ where the Jahn-Teller modes are prohibited by symmetry in the bulk ground-state structure, through quantum confinement effects in the limits of ultrathin films;[61,62] although in this case, strain-induced Jahn-Teller distortions would likely result in larger energetic penalties.

2. *Statistical analysis*

We now evaluate the statistical correlation between the amplitude of the symmetry-adapted modes and the macroscopic $T_{\rm MI}$ and T_N transition temperatures. The physical motivation behind the statistical analysis is to uncover hidden associations between the cooperative atomic displacements and electronic/magnetic phase transitions. The goal is to quantitatively identify structure–functionality relationships that could be rigorously evaluated at the *ab initio* level.

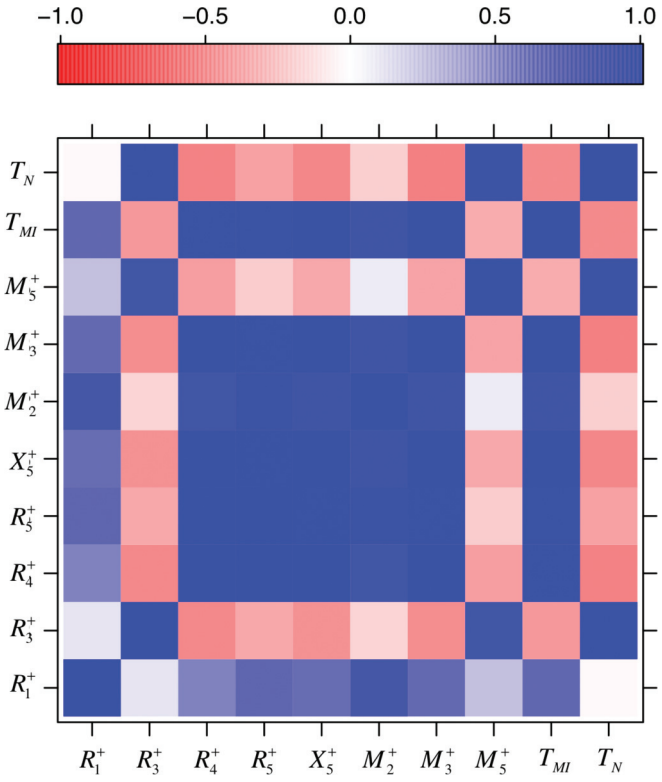

FIG. 6. (Color online) Correlation heat map capturing the degree of linear relationship between unit cell level structural distortion modes and macroscopic transition temperatures, T_{MI}, and T_N in $R\mathrm{NiO_3}$ perovskites. Dark blue (red) indicates a strong positive (negative) correlation and white indicates no statistical correlation between between the two variables. Units for the irreps and temperatures are given in Å and in degrees Kelvin (K), respectively.

We begin by constructing a data set containing seven $R\mathrm{NiO_3}$ nickelates, where each rare-earth nickelate in our set is described using eight distortion modes, T_{MI}, and T_N, resulting in a 7×10 matrix. We scaled the data by subtracting the mean of each column from its corresponding columns (this process is also known as centering), and then divided the centered columns by their standard deviations. To evaluate the degree of linear relationship between the structural distortions, T_{MI}, and T_N, we calculate the sample covariance of the centered and scaled data set as

$$\mathrm{Cov}[X] = \frac{1}{n-1}\sum_{i=1}^{n}(\bar{x}_i)(\bar{x}_j)\,,$$

where $n = 7$ is the total number of $R\mathrm{NiO_3}$ compounds in our data set; $\bar{x}_i$ and $\bar{x}_j$ are the centered and scaled column vectors of our data matrix X, respectively. Results from the covariance analysis are summarized as a correlation heat map in Fig. 6.

A strong positive correlation is found between irreps that describe distortions to the $\mathrm{NiO_6}$ octahedra: M_2^+ (a planar Jahn-Teller mode), M_3^+, X_5^+, R_4^+, and R_5^+ modes. Even though the distortion modes are orthonormal by construction, when they are collectively evaluated for a series of $R\mathrm{NiO_3}$ compounds, our analysis reveals that they (the modes describing the distortions) are statistically *dependent* and coupled. These modes largely describe bond angle distortions and are positively correlated with the electronic transition T_{MI}. The conventional route to describe variations in T_{MI} primarily focus on tolerance factor and *average* ⟨Ni–O–Ni⟩ bond angle, whereby bending of the ⟨Ni–O–Ni⟩ angle further from the ideal case of 180° decreases the bandwidth, promoting the insulating state over the metallic state.[27,34,65] While we recover this behavior, we also identify the unique displacement patterns that geometrically sum to give the aggregate bond angle: irreps M_2^+, M_3^+, X_5^+, R_4^+, and R_5^+ cooperatively act to bend the Ni–O–Ni angle. These five irreps fully describe the *Pnma* crystal structure relative to the cubic phase found in the metallic nickelates at high temperature, reinforcing the concept that the orthorhombic distortions are largely responsible for the bandwidth-controlled transport behavior in nickelates, and hence *prepare* the electronic system for the MIT.

Intriguingly, the R_1^+ CBD distortion, which is the usual signature for CO has only a moderate effect on T_{MI}, indicating that the dominant structural route to engineer the electronic transition may not be solely through *isotropic* bond length distortions. Moreover, *anisotropic* bond distortions obtained with the *a*-type R_3^+ Jahn-Teller mode or the M_5^+ tilting mode do not contribute significantly to T_{MI}. In fact, we find they are *anticorrelated* with the electronic transition temperature (see Fig. 6). Our conclusion to this point is that the geometry (tilt pattern) of the oxygen framework structure is the important atomic scale feature governing the MI transition.

We now shift our attention to the Type-E' antiferromagnetic ordering. Unlike the transport behavior, where the ⟨Ni–O–Ni⟩ bond angle concept appears to be sufficient to explain its variability, the origin of antiferromagnetic ordering is much more complex. Previous high-resolution photoemission measurement[66] and pressure dependent studies[33] of T_N have established the existence of two distinct regimes for $R\mathrm{NiO_3}$ with $T_{\mathrm{MI}} = T_N$ and $T_{\mathrm{MI}} > T_N$, indicating that simple tolerance factor and ⟨Ni–O–Ni⟩ superexchange interaction arguments are insufficient. Lee *et al.* used two-band model and Hartree-Fock theory to classify nickelates with $T_{\mathrm{MI}} = T_N$ as itinerant, whereas those with $T_{\mathrm{MI}} > T_N$ show stronger electron correlation.[48,67] Nonetheless, we are unaware of a unique descriptor available in the literature that captures all the variance in the T_N ordering temperature.

Our analysis reveals the existence of a strong linear relationship between T_N and two irreps, R_3^+ and M_5^+: the three-dimensional Jahn-Teller mode, where in each $\mathrm{NiO_6}$ octahedron four bonds contract and two elongate, and the in-phase tilting mode, respectively. The linear relationship is valid for both $T_{\mathrm{MI}} = T_N$ and $T_{\mathrm{MI}} > T_N$ nickelates (see Fig. 7), indicating that R_3^+ *and* M_5^+ contain additional information that is not captured by either the conventional ⟨Ni–O–Ni⟩ angle or tolerance factor descriptors.

The R_3^+ distortion is more strongly correlated with T_N than the M_5^+, indicating an underlying structural relationship between the long-range antiferromagnetic order and the local and subtle Jahn-Teller bond distortions. We also note that R_3^+ and M_5^+ irreps appear in the monoclinic $P2_1/c$ crystal structure and are not allowed by symmetry in the *Pnma* orthorhombic space group. New insights gained thus far support the potential feasibility of tailoring an isosymmetric $P2_1/c \rightarrow P2_1/c$ phase transition driven by misfit strain, interfaces and surfaces, thermodynamic state variables, and/or

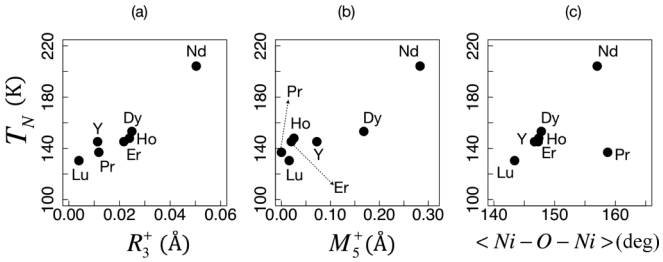

FIG. 7. A strong linear relationship is seen between (a) R_3^+ and the Néel temperature (T_N) with a correlation coefficient of 0.957 and (b) M_5^+ and T_N with a correlation coefficient of 0.916. In (c), we plot the average ⟨Ni–O–Ni⟩ bond angle and T_N to illustrate that the R_3^+ and M_5^+ irreps capture the main variation in T_N for both $T_{MI} = T_N$ and $T_{MI} > T_N$ nickelates compared to the ⟨Ni–O–Ni⟩ bond angle. Experimental data are from Ref. 34.

any combinations thereof, which would result in the preferential enhancement of atomic displacements transforming as R_3^+ and M_5^+ distortions relative to R_1^+.

We conjecture that with deterministic control over the atomic structure, e.g., enhancing R_3^+ relative to other distortion modes, it could be possible to fully decouple T_{MI} from T_N, shifting the equilibrium phase boundaries dividing the metallic/insulating states from the paramagnetic/ordered regions to create nonequilibrium phases. Although it is compelling to extend our interpretation beyond correlation to full causation, we emphasize that first-principles calculations and detailed structural characterization are essential to establish the physical origin underlying the statistical associations we have identified.

B. $Ba_{1-x}K_xBiO_3$ bismuthates

$BaBiO_3$ is a CO insulator which undergoes a series of phase transitions with temperature. At room temperature, it has a monoclinic crystal structure with space group $I2/m$. In the monoclinic $I2/m$ structure, the octahedrally coordinated tetravalent Bi cation charge disproportionates into $Bi^{(4+\delta)+}$ and $Bi^{(4-\delta)+}$. Previous optical conductivity measurements[68] attribute the appearance of an electronic gap in the stoichiometric $I2/m$ phase to structural CBD and octahedra rotations.

Chemical doping of $BaBiO_3$ with potassium by random substitution on the Ba sites, $Ba_{1-x}K_xBiO_3$, produces a sequence of structural and electronic phase transitions. *Increasing* the potassium concentration leads to crystal structures of *higher* symmetry: an orthorhombic $Ibmm$ phase is stable over the range $0.12 \leqslant x < 0.37$. At $x \approx 0.37$, a tetragonal $I4/mcm$ phase is stable and for $0.37 < x < 0.53$ $BaBiO_3$ transforms to $Pm\bar{3}m$ cubic.[69,70] The electronic transport properties also evolve concomitantly with these structural changes; the system transforms from a robust insulating state in the monoclinic phase to semiconducting in the orthorhombic phase and, finally, to a superconducting state in the tetragonal and undistorted cubic phases. Although there are strong evidences supporting an apparent association between structure, doping, and onset of superconductivity, a quantitative assessment of the relationship linking structure to superconductivity is still lacking. Our objective here is to decompose the crystal structure of $Ba_{1-x}K_xBiO_3$ as a function of K doping for $0 \leqslant x \leqslant 0.4$ with emphasis placed on the role of the symmetry-adapted modes and CBD-rotation symmetries.

We decompose the low-symmetry crystal structures of $Ba_{1-x}K_xBiO_3$ across the phase boundaries using five chemical compositions: $BaBiO_3$, $Ba_{0.9}K_{0.1}BiO_3$, $Ba_{0.8}K_{0.2}BiO_3$, $Ba_{0.63}K_{0.37}BiO_3$, and $Ba_{0.60}K_{0.40}BiO_3$, for which high-resolution diffraction data exists.[69,71] When we constructed the hypothetical parent reference structure, we assigned to both K and Ba atoms the same (x,y,z) coordinates and we employed fractional site occupancies to treat the random K substitution on the Ba site. This treatment ensures that the parent structure is $Pm\bar{3}m$ as opposed to any other space group, in which case, the (x,y,z) coordinates for the two cations would be different in the unit cell, i.e., the A-site Wyckoff orbit would split into two, and the space group of the resulting structure would not be the cubic $Pm\bar{3}m$ aristotype.

In practice, the occupancy mode amplitudes are calculated by taking into account the site multiplicity and the fractional occupancy. In this work, for consistency, the fractional site occupancies for the Ba and K atoms in both the hypothetical parent and the experimentally observed distorted structures were kept the same. As a result, $Pm\bar{3}m$ (or for that matter $I2/m$, $Ibmm$, and $I4/mcm$) are treated as random solid solutions, rather than with periodic ordering. Although the static symmetry modes are unable to accurately capture all the nuances of the configurational entropy governing random occupations of Ba/K atoms, the amplitudes of the primary and secondary distortion modes do provide insight into the origin of the doping-dependent structural distortions reported in average structure x-ray diffraction measurements. This approach is particularly useful to build an understanding of the interplay of doping and structure in the bismuthates, because computational modeling of $Ba_{1-x}K_xBiO_3$ phases present nontrivial challenges due to the random nature of the solid solution. Such configurations necessitate the construction of large supercells and may require computationally demanding hybrid functionals to accurately reproduce the electronic structure.[70]

The results from our analysis are summarized in Fig. 8. The $I2/m$ structure is described by four irreps R_1^+, R_3^+, R_4^+, and R_5^+, which capture the CBD, a Jahn-Teller distortion, out-of-phase octahedral rotations, and out-of-phase bond stretching, respectively. Although the $I2/m$ monoclinic symmetry is maintained at small doping, as with $Ba_{0.9}K_{0.1}BiO_3$, our mode decomposition analysis reveals that the amplitude of the R_3^+ distortion vanishes completely. The relative amplitudes of the R_1^+ CBD and out-of-phase octahedral rotation modes also decrease, whereas the amplitude of the out-of-phase bending distortion increases [see Fig. 8 (inset)].

With further increase in K concentration, for example, in $Ba_{0.8}K_{0.2}BiO_3$, the crystal structure becomes orthorhombic $Ibmm$. Interestingly, even in the absence of the CBD distortion (R_1^+), which we find has zero amplitude at $x = 0.2$, the electronic structure remains insulating.[70] At the same time, the amplitude of the R_5^+ distortion continues to increase in the presence of out-of-phase octahedral rotations, described by R_4^+. Upon further increase in K, the amplitude of R_5^+

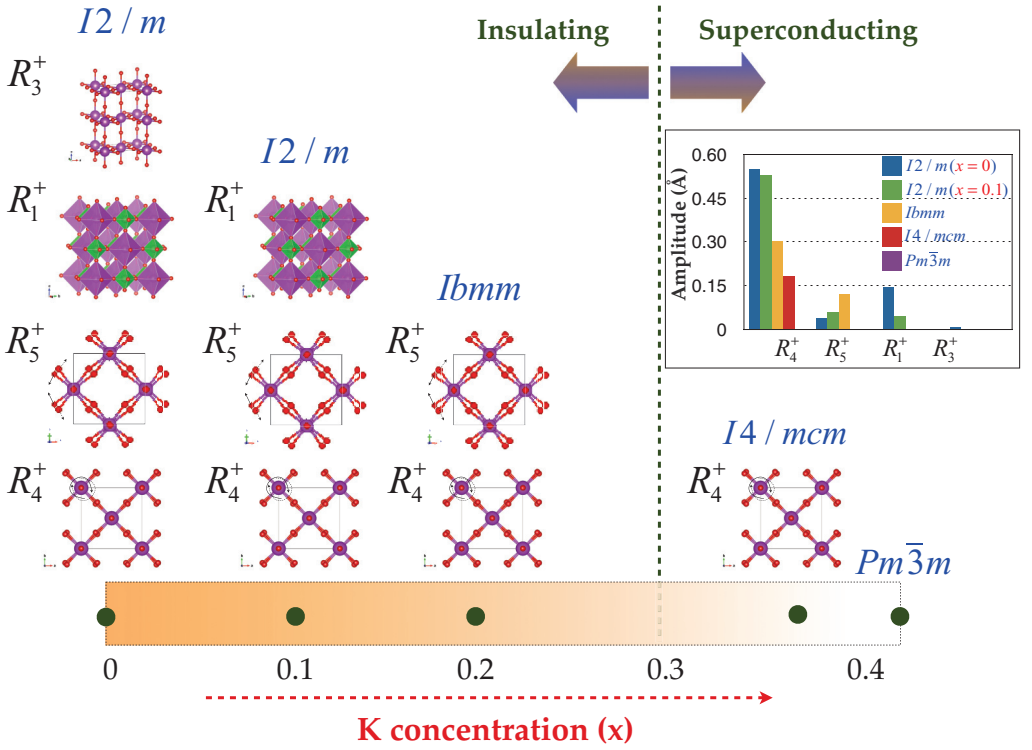

FIG. 8. (Color online) Relationship between crystal symmetry and structural distortions in $Ba_{1-x}K_xBiO_3$ as a function of *A*-site doping. The number of symmetry unique structural modes decreases with increasing K concentration. Pure $BaBiO_3$ is described by four modes: R_1^+, R_3^+, R_4^+, and R_5^+. As the concentration of K increases, the Jahn-Teller R_3^+ mode disappears rapidly, followed by loss of the three-dimensional CBD R_1^+. The bar graph (inset) shows quantitatively in units of angstroms the change in amplitude of the structural modes observed in each space group.

distortion disappears completely, yielding tetragonal $I4/mcm$ $Ba_{0.63}K_{0.37}BiO_3$ with only the R_4^+ irrep, which corresponds to modes with out-of-phase octahedral tilting at reduced amplitude. Across this structural transition, the compound becomes metallic and superconducting[69] with a critical transition temperature of 27 K. Finally, for $x \sim 0.4$, the superconducting phase is also stable in the cubic $Pm\bar{3}m$ structure without any octahedral rotations or distortions.

An outstanding question concerning the electronic phase diagram of $Ba_{1-x}K_xBiO_3$ is the presence of the wide semiconducting or insulating region with doping. Our mode decomposition analysis provides an alternative interpretation of the phase diagram. In $Ba_{1-x}K_xBiO_3$, the octahedral rotations corresponding to irrep R_4^+ is found to be the primary distortion and it couples with other secondary distortions, namely R_3^+, R_1^+, and R_5^+ depending on the concentration of K. Particularly, we focus on the R_4^+ and R_5^+ distortions. Even though R_5^+ is a secondary distortion, it has a significant nonzero amplitude (0.12 Å) near the insulator–superconductor phase boundary. To the best of our knowledge, no previous study has examined the role of primary and secondary distortions on the insulator–superconductor phase boundary.

In the insulating regime, the amplitude of R_4^+ monotonically decreases with increasing K. On the other hand, the amplitude of R_5^+ distortion is found to monotonically increase with K. The trend in R_4^+ and R_5^+ distortion pattern bears a remarkable resemblance with the evolution in the dielectric response reported by Nishio *et al.* semiconducting $Ba_{1-x}K_xBiO_3$ on single-crystal samples.[72] Nishio *et al.* identified two features in their optical spectra: the first was associated with the excitation from the lower Peierls band to the bipolaron defect state, which showed an increase in intensity with K concentration similar to the increase in amplitude of R_5^+. The second feature was assigned with the magnitude of the Peierls gap, which decreased with increasing K concentration like R_4^+. Our analysis suggests that the stability of the polaronic defects and the magnitude of the gap in the orthorhombic bismuthates may be intimately tied to the amplitude of the R_4^+ (rotations) and R_5^+ (bond stretching) distortions.

Electronic structure calculations would allow us to unravel this association and glean insights into the persistence of wide semiconducting or insulating regions in $Ba_{1-x}K_xBiO_3$ compounds. To do so, we propose a computational experiment to test the relationship between octahedral distortions and the optical spectra. One could "freeze-in" the R_4^+ (or alternatively R_5^+) distortion and map the energy landscape as a function of the amplitudes of R_5^+ (or the corresponding R_4^+) distortion. For each structure, the complex frequency-dependent dielectric function would be computed following the computational approach of Franchini *et al.*, who has successfully demonstrated that hybrid functionals are capable of describing both octahedral distortions and the complex electronic states.[70] This would permit the independent assessment of the relative role of R_4^+ and R_5^+ distortions

on the closing of the Peierls gap and the stability of the bipolaron defect states. While our computational proposal may appear seemingly simple, this is by no means a trivial set of computations.

VI. SUMMARY

We applied group theoretical methods to evaluate the interplay between octahedral rotations and electronic charge ordering, which we parameterized structurally as octahedral "breathing" or cooperative bond length distortions through irreducible representations of the aristotype space group. We enumerated the possible space groups available to perovskites from the intersection of these distortions. This crystallographic data should prove useful for experimental structure refinements or serve as a well-defined set of symmetry-unique structures for which the stability of transition metal compounds susceptible to charge ordering may be evaluated with first-principles total energy methods.

With this information, we combined structural mode decomposition techniques with statistical methods to extract unbiased structure-property relationships from available experimental diffraction data on representative charge ordering oxides. The crystal structures of perovskite nickelates and bismuthates were decomposed in terms of symmetry-adapted distortion-modes and the evolution in the amplitude of each mode tracked as a function of an external chemical parameter. We illustrated that this alternative set of descriptors provides a useful construct beyond the traditional tolerance factor paradigm found in perovskites to understand the atomic scale origin of physical properties, specifically how unit cell level modifications correlate with macroscopic functionality.

Our statistical analysis uncovered previously unappreciated relationships that may be harnessed for electronic structure by design, some of which are being carried out within our group and will be reported later. We emphasize that the application of statistics to the decompositions does not require solely experimental data; the analysis may be performed with computationally obtained data alone. Importantly, the relationships established with these techniques may be cross-validated by the construction of hybrid data sets, which combine theoretical results with experiment data, making it possible to extract and validate new insight into the material physics of oxides with correlated electrons. We anticipate that this approach will spawn a number of additional studies in diverse crystal classes since it is immediately generalizable: the synergy of applied group theoretical methods with statistical analysis and subsequent first-principles calculations provides a platform to achieve rational structure-driven design of complex materials.

ACKNOWLEDGMENTS

P.V.B. was supported by The Defense Advanced Research Projects Agency (DARPA) under Grant No. N66001-12-4224. J.M.R. was supported by the US Office of Naval Research (ONR), under Grant No. N00014-11-1-0664. The views, opinions, and/or findings reported here are solely those of the authors and do not represent official views of DARPA or ONR. We thank our group members, D. Puggioni and A. Cammarata, for useful discussions.

*jrondinelli@coe.drexel.edu

[1]N. A. Benedek, A. T. Mulder, and C. J. Fennie, J. Solid State Chem. **195**, 11 (2012).

[2]C. J. Howard and H. T. Stokes, Acta Crystallogr. Sect. B **54**, 782 (1998).

[3]E. Canadell, M.-L. Doublet, and C. Iung, *Orbtial Approach to the Electronic Structure of Solids* (Oxford University Press, New York, 2012).

[4]A. J. Millis, P. B. Littlewood, and B. I. Shraiman, Phys. Rev. Lett. **74**, 5144 (1995).

[5]M. A. Carpenter and C. J. Howard, Acta Crystallogr. Sect. B **65**, 134 (2009).

[6]M. A. Carpenter and C. J. Howard, Acta Crystallogr. Sect. B **65**, 147 (2009).

[7]J. B. Goodenough and F. Rivadulla, Mod. Phys. Lett. B **19**, 1057 (2005).

[8]M. B. Salamon and M. Jaime, Rev. Mod. Phys. **73**, 583 (2001).

[9]J. B. Goodenough, Rep. Prog. Phys. **67**, 1915 (2004).

[10]J. Matsuno, T. Mizokawa, A. Fujimori, Y. Takeda, S. Kawasaki, and M. Takano, Phys. Rev. B **66**, 193103 (2002).

[11]The MI transition results from electronic localization, which can be intrinsic and electrostatic in nature (electron-electron repulsion), or extrinsic, due to defects or disorder.

[12]Y. Quan, V. Pardo, and W. E. Pickett, Phys. Rev. Lett. **109**, 216401 (2012).

[13]H. Park, A. J. Millis, and C. A. Marianetti, Phys. Rev. Lett. **109**, 156402 (2012).

[14]A. Cammarata and J. M. Rondinelli, Phys. Rev. B **86**, 195144 (2012).

[15]Not all charge-ordering transitions require an concomitant change in structure, see, for example, the case of $LaSr_2Fe_3O_{12}$.

[16]T. Saha-Dasgupta, Z. S. Popović, and S. Satpathy, Phys. Rev. B **72**, 045143 (2005).

[17]T. Mizokawa, D. I. Khomskii, and G. A. Sawatzky, Phys. Rev. B **60**, 7309 (1999).

[18]The list is for *B*-site ordered perovskites where breathing distortions is not due to the spontaneous electron instability, but present because of ordered arrangement of *B*-site element.

[19]For the irreducible representation matrices, we employed 1988 version for special *k* points and 2011 version for the nonspecial *k* points as implemented in ISOTROPY and ISODISTORT.

[20]This distortion is not a Jahn-Teller elongation of the octahedra, because the equatorial oxygen of a single octahedron either all elongate (contract) in the same direction; a Jahn-Teller distortion is rather seen as a two-in-two-out distortion of the equatorial oxygen atoms.

[21] G. King and P. M. Woodward, J. Mater. Chem. **20**, 5785 (2010).

[22] B. J. Campbell, H. T. Stokes, D. E. Tanner, and D. M. Hatch, J. Appl. Crystallogr. **39**, 607 (2006).

[23] C. J. Howard and H. T. Stokes, Acta Crystallogr. Sect. A **61**, 93 (2005).

[24] C. J. Howard and H. T. Stokes, Acta Crystallogr. Sect. B **60**, 674 (2004).

[25] H. T. Stokes, E. H. Kisi, D. M. Hatch, and C. J. Howard, Acta Crystallogr. Sect. B **58**, 934 (2002).

[26] A. M. Glazer, Acta Crystallogr. Sect. B **28**, 3384 (1972).

[27] J. B. Torrance, P. Lacorre, A. I. Nazzal, E. J. Ansaldo, and C. Niedermayer, Phys. Rev. B **45**, 8209 (1992).

[28] S. J. May, J.-W. Kim, J. M. Rondinelli, E. Karapetrova, N. A. Spaldin, A. Bhattacharya, and P. J. Ryan, Phys. Rev. B **82**, 014110 (2010).

[29] J. M. Rondinelli, S. J. May, and J. W. Freeland, MRS Bulletin **37**, 261 (2012).

[30] J. Chakhalian, J. M. Rondinelli, J. Liu, B. A. Gray, M. Kareev, E. J. Moon, N. Prasai, J. L. Cohn, M. Varela, I. C. Tung, M. J. Bedzyk, S. G. Altendorf, F. Strigari, B. Dabrowski, L. H. Tjeng, P. J. Ryan, and J. W. Freeland, Phys. Rev. Lett. **107**, 116805 (2011).

[31] A. Blanca-Romero and R. Pentcheva, Phys. Rev. B **84**, 195450 (2011).

[32] A. V. Boris, Y. Matiks, E. Benckiser, A. Frano, P. Popovich, V. Hinkov, P. Wochner, M. Castro-Colin, E. Detemple, V. K. Malik, C. Bernhard, T. Prokscha, A. Suter, Z. Salman, E. Morenzoni, G. Cristiani, H.-U. Habermeier, and B. Keimer, Science **332**, 937 (2011).

[33] J.-S. Zhou, J. B. Goodenough, and B. Dabrowski, Phys. Rev. Lett. **95**, 127204 (2005).

[34] G. Catalan, Phase Trans. **81**, 729 (2008).

[35] J. B. Goodenough, in *Structure and Bonding, Localized to Itinerant Electronic Transitions in Perovskite Oxides*, Vol. 98, edited by J. B. Goodenough (Spring-Verlag, Berlin, Heidelberg, 2001).

[36] J. M. Perez-Mato, D. Orobengoa, and M. I. Aroyo, Acta Crystallogr. Sect. A **66**, 558 (2010).

[37] M. T. Dove, Am. Mineral. **82**, 213 (1997).

[38] O. Diéguez, O. E. González-Vázquez, J. C. Wojdeł, and J. Íñiguez, Phys. Rev. B **83**, 094105 (2011).

[39] R Development Core Team, *R: A Language and Environment for Statistical Computing*, (R Foundation for Statistical Computing, Vienna, Austria, 2012).

[40] D. Sarkar, *Lattice: Multivariate Data Visualization with R* (Springer, New York, 2008).

[41] See Supplemental Material at http://link.aps.org/supplemental/10.1103/PhysRevB.88.054101 for accessing the R script.

[42] M. L. Medarde, J. Phys.: Condens. Matter **9**, 1679 (1997).

[43] J. A. Alonso, J. L. García-Muñoz, M. T. Fernández-Díaz, M. A. G. Aranda, M. J. Martínez-Lope, and M. T. Casais, Phys. Rev. Lett. **82**, 3871 (1999).

[44] The first origin choice is only used for notation purposes to avoid confusion. Our actual mode-decomposition was performed using $P2_1/n$ space group as reported in the literature.

[45] M. Medarde, P. Lacorre, K. Conder, F. Fauth, and A. Furrer, Phys. Rev. Lett. **80**, 2397 (1998).

[46] V. I. Anisimov, D. Bukhvalov, and T. M. Rice, Phys. Rev. B **59**, 7901 (1999).

[47] I. I. Mazin, D. I. Khomskii, R. Lengsdorf, J. A. Alonso, W. G. Marshall, R. M. Ibberson, A. Podlesnyak, M. J. Martínez-Lope, and M. M. Abd-Elmeguid, Phys. Rev. Lett. **98**, 176406 (2007).

[48] B. Lau and A. J. Millis, Phys. Rev. Lett. **110**, 126404 (2013).

[49] J. A. Alonso, M. J. Martínez-Lope, M. T. Casais, J. L. García-Muñoz, and M. T. Fernández-Díaz, Phys. Rev. B **61**, 1756 (2000).

[50] M. Medarde, M. T. Fernández-Díaz, and P. Lacorre, Phys. Rev. B **78**, 212101 (2008).

[51] J. L. García-Muñoz, M. A. G. Aranda, J. A. Alonso, and M. J. Martínez-Lope, Phys. Rev. B **79**, 134432 (2009).

[52] A. Munoz, J. Alonso, M. Martinez-Lope, and M. Fernandez-Diaz, J. Solid State Chem. **182**, 1982 (2009).

[53] A. T. Mulder, N. A. Benedek, J. M. Rondinelli, and C. J. Fennie, Adv. Funct. Mater., doi: 10.1002/adfm.201300210.

[54] V. Dvořák and J. Petzelt, Phys. Lett. A **35**, 209 (1971).

[55] A. P. Levanyuk and D. G. Sannikov, Sov. Phys. Usp. **17**, 199 (1974).

[56] J. Tolédano and P. Tolédano, *The Landau Theory of Phase Transitions* (World Scientific Publishing Co. Pte. Ltd., Singapore, 1987).

[57] J. M. Perez-Mato, P. Blaha, K. Schwarz, M. Aroyo, D. Orobengoa, I. Etxebarria, and A. García, Phys. Rev. B **77**, 184104 (2008).

[58] I. Etxebarria, J. M. Perez-Mato, and P. Boullay, Ferroelectrics **401**, 17 (2010).

[59] N. A. Benedek and C. J. Fennie, Phys. Rev. Lett. **106**, 107204 (2011).

[60] A. Stroppa, P. Barone, P. Jain, J. M. Perez-Mato, and S. Picozzi, Adv. Mater. **25**, 2284 (2013).

[61] J. Chakhalian, J. M. Rondinelli, J. Liu, B. A. Gray, M. Kareev, E. J. Moon, N. Prasai, J. L. Cohn, M. Varela, I. C. Tung, M. J. Bedzyk, S. G. Altendorf, F. Strigari, B. Dabrowski, L. H. Tjeng, P. J. Ryan, and J. W. Freeland, Phys. Rev. Lett. **107**, 116805 (2011).

[62] J. W. Freeland, J. Liu, M. Kareev, B. Gray, J. W. Kim, P. Ryan, R. Pentcheva, and J. Chakhalian, Europhys. Lett. **96**, 57004 (2011).

[63] H. Chen, D. P. Kumah, A. S. Disa, F. J. Walker, C. H. Ahn, and S. Ismail-Beigi, Phys. Rev. Lett. **110**, 186402 (2013).

[64] I. C. Tung, P. V. Balachandran, J. Liu, B. A. Gray, E. A. Karapetrova, J. H. Lee, J. Chakhalian, M. J. Bedzyk, J. M. Rondinelli, and J. W. Freeland (unpublished).

[65] X. Obradors, L. M. Paulius, M. B. Maple, J. B. Torrance, A. I. Nazzal, J. Fontcuberta, and X. Granados, Phys. Rev. B **47**, 12353 (1993).

[66] I. Vobornik, L. Perfetti, M. Zacchigna, M. Grioni, G. Margaritondo, J. Mesot, M. Medarde, and P. Lacorre, Phys. Rev. B **60**, R8426 (1999).

[67] S. B. Lee, R. Chen, and L. Balents, Phys. Rev. B **84**, 165119 (2011).

[68] M. A. Karlow, S. L. Cooper, A. L. Kotz, M. V. Klein, P. D. Han, and D. A. Payne, Phys. Rev. B **48**, 6499 (1993).

[69] M. Braden, W. Reichardt, E. Elkaim, J. P. Lauriat, S. Shiryaev, and S. N. Barilo, Phys. Rev. B **62**, 6708 (2000).

[70] C. Franchini, G. Kresse, and R. Podloucky, Phys. Rev. Lett. **102**, 256402 (2009).

[71] S. Pei, J. D. Jorgensen, B. Dabrowski, D. G. Hinks, D. R. Richards, A. W. Mitchell, J. M. Newsam, S. K. Sinha, D. Vaknin, and A. J. Jacobson, Phys. Rev. B **41**, 4126 (1990).

[72] T. Nishio, J. Ahmad, and H. Uwe, Phys. Rev. Lett. **95**, 176403 (2005).